Journal of Hazardous Materials 173 (2010) 211–222

Contents lists available at ScienceDirect

Journal of Hazardous Materials

journal homepage: www.elsevier.com/locate/jhazmat

Development of surface functionalized activated carbon fiber for control of NO and particulate matter

Rajveer Singh Rathore [a], Dhananjay Kumar Srivastava [b], Avinash Kumar Agarwal [b], Nishith Verma [c,*]

[a] Environmental Engineering and Management Program, Indian Institute of Technology Kanpur, Kanpur 208016, India
[b] Department of Mechanical Engineering, Indian Institute of Technology Kanpur, Kanpur 208016, India
[c] Department of Chemical Engineering, Indian Institute of Technology Kanpur, Kanpur 208016, India

ARTICLE INFO

Article history:
Received 14 April 2009
Received in revised form 25 July 2009
Accepted 15 August 2009
Available online 22 August 2009

Keywords:
Activated carbon fiber
Surface functionalization
Engine emission
NO
Particulate matter
Diesel particulate filter

ABSTRACT

This study investigates the development and potential application of activated carbon fibers (ACF) functionalized with ammonia for control of NO and particulate matter (PM) in diesel engine exhaust. A tubular reactor packed with ACF was used to experimentally study the oxidation of NO at room temperature. Tests were conducted at ACF functionalized with three aqueous ammonia concentrations (3, 5, 10 M), three basic reagents (ammonia, pyridine, amine) and three NO concentrations (100, 300, 500 ppm). After offline investigation, the ACF-packed tubular reactor was installed downstream of the engine's exhaust to ascertain the PM capturing efficiency of ACF. The experimental conditions for PM removal included three weights of ACF (2, 3.5, 4.5 g), three engine loads (0, 25, 50 Nm) and three temperatures (150, 300, 450 °C). The maximum 70% conversion for NO was obtained at NO concentration of 300 ppm for ACF functionalized with 5 M ammonia, whereas maximum 90% reduction in PM was observed at engine load of 25 Nm and 450 °C. The study shows significant potential for the ACF based filters in capturing both homogeneous and heterogeneous pollutants emitted from automobiles. Our previously developed transport model incorporating the mechanism for the oxidation of NO was also used to explain the experimental data.

1. Introduction

The adverse impact of nitrogen oxide (NO) and particulate matter (PM) emitted from diesel engines on atmospheric air quality and human health is well recognized [1,2]. The selective catalyst reduction (SCR) of NO using ammonia, and oxidation at room temperature are the two widely used techniques to control emission of NO from flue gases. V_2O_5 supported on TiO_2 catalyst and other noble metals are preferred for SCR. However, these catalysts may be prohibitively expensive. Majority of PM emitted from diesel engines are nanoparticles, largely consisting of carbon soot, condensed ash from the lubricating oil, condensate of HC and sulfuric acid, and also substantial amount of metallic compounds [3–5]. With regard to the control of PM emitted from diesel engines, a variety of diesel particulate filters (DPF) have been developed in the last decade which essentially rely on the basic principle of collection of the particles on a substrate and their simultaneous oxidation [6–8]. Yet, there are concerns regarding particulate capturing efficiency and regeneration of these filters.

The focus of the present study is on the development of activated carbon fiber (ACF) for the combined removal of NO and PM emitted from the diesel engine. In recent times, ACF has been the interest of a numerous research studies due to the recognition of its multi-facet roles as an adsorbent, a catalyst as well as support to metallic catalyst in the context of air pollution control [9–13]. In the present study, the surface of ACF was modified by incorporating basic functional groups with a view to improving its affinity towards NO for the subsequent oxidation to NO_2. In this context, there are also a number of studies pertaining to the surface functionalization of ACF or active carbons (AC) by using basic agents such as NH_3 and amines, either in liquid or vapor phase [14–17]. The surface functionalization yields in the incorporation of many functional groups such as C═N, C—N, cyclic amide and nitrile group, which is shown to significantly improve the adsorption capacity of the functionalized ACF in comparison to that of the untreated ACF. Nitrogen doping of ACF by the chemical vapor deposition (CVD) of pyridine has also been carried out [18]. The equilibrium NO concentration on the nitrogen-doped ACF is observed to significantly increase in comparison to the untreated ACF.

From the literature survey, it may also be inferred that most of the studies pertain to the applicability of surface functionalized ACF under equilibrium conditions. The present study envisages the development of functionalized ACF for control of NO under dynamic

* Corresponding author. Tel.: +91 512 2596124; fax: +91 512 2590104.
E-mail address: nishith@iitk.ac.in (N. Verma).

0304-3894/$ – see front matter © 2009 Elsevier B.V. All rights reserved.
doi:10.1016/j.jhazmat.2009.08.071

(flow) conditions. In our previous studies, it has been experimentally demonstrated that the true performance of an adsorbent for a gaseous species is reflected under flow conditions taking into considerations different mass transfer and kinetic rates, which are absent during equilibrium conditions [9–12].

In the following section, the experimental set-up and procedure used in the study for the preparation of surface functionalized ACF are described. The discussion of the data pertaining to the NO oxidation is presented next. The description of the experimental set-up for ascertaining the efficiency of the prepared ACF in capturing PM from the exhaust of a diesel engine and the data thereof are discussed in the subsequent section. Finally, conclusions are made.

2. NO oxidation

2.1. Experimental

2.1.1. ACF preparation (activation and carbonization)

The raw carbonaceous fibers based on the phenolic resin precursor were procured from Nippon Kynol Inc., Japan. The ACFs were prepared first by carbonizing the raw fibers in an inert atmosphere and then by activation using steam as an oxidizing agent. The details of the experimental set-up and procedure used for activation and carbonization may be obtained from our previous work and are not reproduced here for brevity [11]. In brief, the set-up mainly consisted of the two co-axially mounted tubes made of inconel, which were horizontally placed in a ceramic furnace at a high temperatures ($T \sim 1373$ K). The inner tube ($L = 32$ cm, I.D. = 0.8 cm) was circumferentially perforated with holes of 0.05 mm diameter and 1 cm apart. ACF was wrapped over the perforated section of the inner tube, one end of which was connected to the gas inlet, while the other end was closed, so that the incoming gas flowed into the tubes radially outward through the perforations, the wrapped fiber, and then the outer tube before exiting through the vent.

For carbonization, the raw samples were pyrolyzed at 1273 K. The samples were slowly heated upto the desired temperature at a constant rate of ~3 °C/ min under a small N_2 flow rate (300 sccm). Carbonization was carried out for 90 min. Following carbonization, activation was carried out for 120 min. After activation, the samples were cooled to the room temperature at a rate of 3 °C/ min under a small N_2 flow rate (300 sccm).

2.1.2. ACF surface functionalization

The surface of the ACF samples was functionalized by impregnating them with several basic reagents (ammonia, pyridine, amine, etc.), either in the liquid or vapor phase. Fig. 1a is the schematic of the experimental set-up used in the study of liquid phase impregnation. ACF was wrapped over a perforated glass tube, which in turn was mounted inside a conical flask with provisions made for the water inlet and outlet. One end of the tube was closed. The outer surface of the tube was perforated with holes of diameter 0.1 mm at the center-to-center distance of 4 mm. With the aid of a peristaltic pump, the alkaline solution in a glass container was continuously re-circulated to the inlet of the tube, as shown in the schematic (Fig. 1a). It was observed that this method (impregnation under flow condition) resulted in uniform dispersion of the reagents in ACF as compared to other traditional methods like impregnation by continuously stirring ACF in solution or leaving ACF in the solution under batch condition without stirring. Additionally, the total time of impregnation was considerably reduced (approximately 12 h) as against 20–24 h in other arrangements.

The aqueous solutions of three different basic reagents (ammonia, pyridine, and amine) were used for impregnation in the study. The impregnation time was 12 h, whereas the temperature of the impregnating solution was set between 60 and 80 °C. Tests were conducted at three different aqueous ammonia concentrations (3, 5, and 10 M). The weight of ACF wrapped over the perforated tubular reactor was approximately 5 g during each impregnation run. The flowrate of the reagents was set constant at 20 cm^3 per min by setting the speed of the pre-calibrated peristaltic pump.

Fig. 1b is the schematic of the arrangement used for the vapor phase impregnation of ACF. Nitrogen as a carrier gas was bubbled through a bubbler containing the aqueous alkaline solution of the reagent for impregnation. The temperature of the bubbler was set constant at 40–60 °C with the aid of a Freon refrigeration unit, depending upon the required concentration of the vapor in the carrier gas. The concentration of the aqueous solution was the same as that used in the liquid phase impregnation. Thus, the vapor phase concentration in the carrier gas was set by the saturation vapor pressure of the liquid. For example, 5 M liquid ammonia concentration at 40 °C corresponds to approximately 15% (v/v) vapor phase concentration in nitrogen. The reagent laden nitrogen was passed at a constant flowrate of 100 sccm (cc per min measured at standard conditions) through a perforated tubular reactor wrapped with ACF. The weight of ACF was approximately 5 g. The geometrical configuration of the reactor is similar to that used for activation step. The contact (impregnation) temperature was set at 750 °C, whereas contact time was one hour. The vapor–solid contact resulted in the attachment of N-containing functional groups over the ACF surface. After impregnation, the system was allowed to cool down to room temperature while being purged with nitrogen.

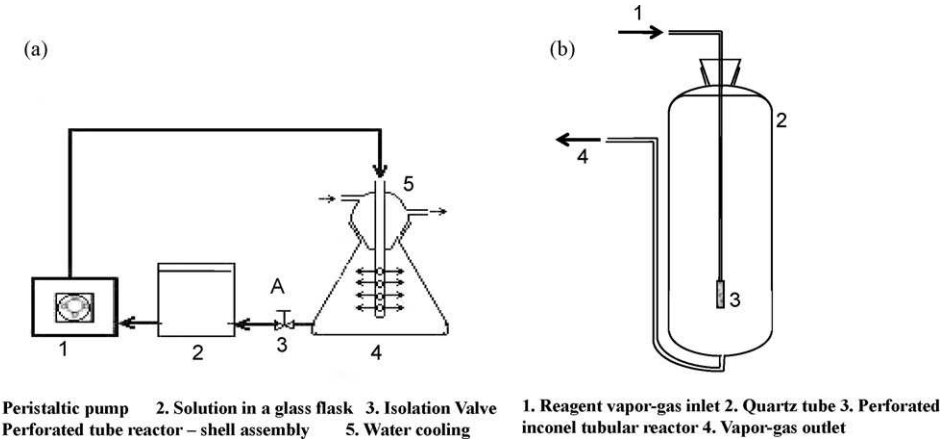

1. Peristaltic pump 2. Solution in a glass flask 3. Isolation Valve 4. Perforated tube reactor – shell assembly 5. Water cooling

1. Reagent vapor-gas inlet 2. Quartz tube 3. Perforated inconel tubular reactor 4. Vapor-gas outlet

Fig. 1. (a) Schematic of the experimental set-up for aqueous phase surface functionalization of ACF. (b) Schematic of the experimental set-up for vapor phase surface functionalization of ACF.

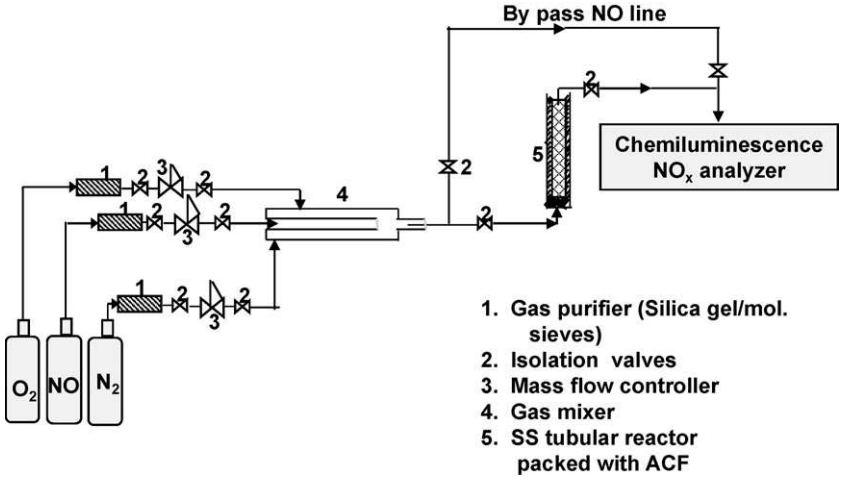

Fig. 2. Schematic of experimental set-up for NO oxidation over ACF.

2.1.3. Experimental set-up for NO oxidation over ACF

Fig. 2 is the schematic of the experimental set-up used to study the oxidation of NO by ACF. The set-up may be assumed to consist of three sections: (a) gas-mixing, (b) test and (c) analytical sections. The gas-mixing section included a gas-mixing chamber (L = 135 mm and I.D. = 25 mm) made of stainless steel (SS) for preparing the gaseous mixture of NO, O_2 and N_2 at predetermined concentrations. Three electronic mass flow controllers (Make: Bronkhorst; Model: PSFIC-I, Netherlands) were used to control and measure the flow rates of three gaseous streams. The various gas streams were purified using silica gel to remove any impurities or moisture in the gas. There was an option of bypassing the gaseous mixture directly to the analytical section for calibration as well as for the measurement of the inlet concentration of the gaseous mixture entering the reactor.

The test section consisted of the two co-axially mounted tubes made of inconel, similar to that ones used in the activation study. The inner tube (L = 150 cm, I.D. = 14 mm) was circumferentially perforated with holes of 0.1 mm diameter and 10 mm apart. ACF was wrapped over the perforated section of the inner tube, one end of which was connected to the gas inlet, while the other end was closed, so that the incoming gas flowed into the tubes radially outward through the perforations, the wrapped fiber, and then into the outer tube before exiting through the vent. The heating of the tubular reactor was provided using a tubular furnace (1000 W). The temperature of the furnace was controlled with the aid of a PID temperature controller (Make: Fuji Electric Co., Japan; Model: PXZ-4,). The analytical section consisted of Chemiluminescence NO_x analyzer (Thermo electron Co. USA; Model: 42C) to measure the concentrations of NO and NO_2.

The experimental conditions for the oxidation tests included varying weight of ACF (0.25, 0.5, 1 g), NO concentrations (100, 300 and 500 ppm) and flowrates of the gaseous mixture (100, 200, 500 sccm). The O_2 concentration and reaction temperature were set at 20% and 40 °C, respectively, for all test runs.

2.2. Surface characterization data

As pointed out earlier in the text, various basic reagents were used to functionalize ACF. However, ACF functionalized using ammonia was found to be most effective in the oxidation of NO. The discussion of most of the results in this study is therefore limited to those pertaining to the ammonia functionalized ACF, for brevity. Table 1 presents the specific surface area and pore volume of as-received ACF samples and those prepared for NO oxidation.

Table 1
Surface characteristics calculated using BET equations[a] for commercial and ammonia treated ACF samples.

Sample	S_g (m^2/g)	V_g (cm^3/g)
ACF	1204	0.7
ACF-NH_3/3M	1190	0.49
ACF-NH_3/5M	1199	0.53
ACF1-NH_3/10M	1195	0.52

S_g: Specific surface area calculated from the BET equation. V_g: Total pore volume calculated from the BET equation.

[a] The parameter estimations are done by the adsorption isotherms of N_2 gas.

The BET area and micro-pore volume of the ammonia treated ACF samples at 3, 5, and 10 M concentrations were found to be approximately the same (1190, 1199 and 1195 m^2/g, respectively). The total pore volume of these samples was measured to be 0.49, 0.53 and 0.52 cm^3/g respectively. The above results suggest that increase in ammonia concentration at room temperature does not affect the BET area and the pore volume of ACF.

The FTIR analysis of ammonia treated ACF samples was carried out for ascertaining various nitrogen and other functional groups. Fig. 3 describes the FTIR spectra of ACF samples with and without NH_3 treatment. Changes in the chemical surface groups due to ammonia treatment of ACF may be observed from the figure.

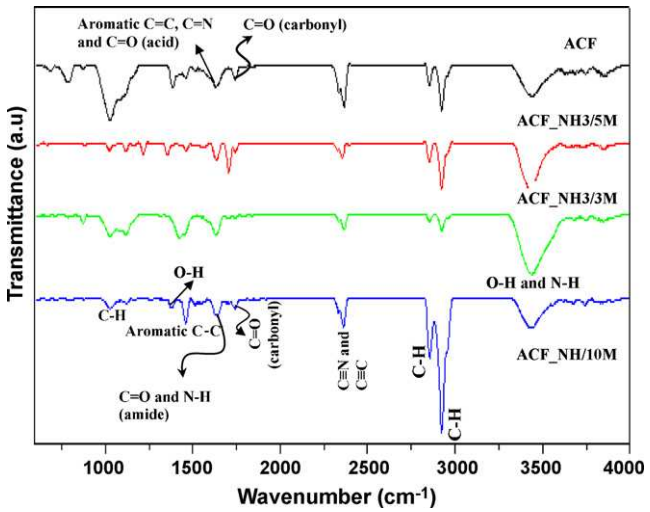

Fig. 3. FTIR spectra of NH_3 impregnated ACF samples.

The peak observed at ~3428 cm^{-1} for untreated corresponds to OH stretching of carboxylic acid and phenolic O-H of aromatic rings, respectively. The peaks at ~2936 and 2852 cm^{-1} represent the C-H stretching of aromatic ring. The bands at ~2360 and 2329 cm^{-1} correspond to C≡N (nitrile group) and C≡C stretching.

In the case of ammonia treated ACF, the band at ~3428 cm^{-1} corresponds to N–H stretching of amide. The peak at 1748 cm^{-1} corresponds to carbonyl group. In the case of raw ACF the peak ~1638 cm^{-1} corresponds to C=O stretching of carboxylic acid and aromatic C=C and C=N stretching, whereas in the case of ammonia treated ACF there is a small shift in the band observed at ~1633 cm^{-1}, which represents the enhancement of C=O stretching and N–H bending of amide functionality. The peak at 1468 cm^{-1} corresponds to aromatic C–C stretching and that at 1380 cm^{-1} corresponds to O–H bending. In addition, small vibrations present below 900 cm^{-1} may be due to the bending vibration of C–H bonds of aromatic rings.

There are three clarifications in order. (1) These N-containing groups possess an isolated electron in their nitrogen atom. Due to the presence of this electron, ACF surface becomes alkaline, which has strong affinity to acidic species such as NO_x and SO_x. In the present work, the presence of N-containing functional groups in ACF surface resulted in the enhanced NO adsorption via chemisorptions and/or catalytic oxidation. The following mechanism was proposed for impregnation of ACF by NH_3 [16].

$$C_nH_xO_y + 2NH_3 \rightarrow [N \ldots C_nH_xO_{y-3} \ldots N] + 3H_2O$$

(2) After treating ACF with ammonia, we detect extra bond due to amide group, along with C–H aromatic bond and carboxylic group. Important to point out is that the latter stretching are also present in non-functionalized ACF. Therefore, we can conclude that some bonds stretching for untreated ACF as well as ammonia treated ACF will appear at the same wave number, which may have to be discerned carefully. (3) Since the substrate ACF is impregnated with the same impregnating solution (ammonia) of different concentrations, various surface groups appearing for the three samples are the same. The groups also appear at nearly the same respective wave number. Any error in this respect is attributed due to the recording atmosphere or instrumental accuracy. It is also important to point out that the relative magnitude of the intensity observed in the FTIR spectra should not be construed as the proportionate amount (number density) of the respective surface group present in the samples. It only reflects the probability of finding the particular surface group [19].

2.3. NO oxidation data

2.3.1. Non-functionalized ACF

The experimental data obtained during the oxidation of NO on ACF are presented in Fig. 4. The transient data obtained using the NO_x analyzer represent the breakthrough curves (transient response of the adsorbent bed to a step-change in the influent concentration) for NO and NO_2 during the oxidation of NO. The steady-state conversion of NO is defined as $(C_{inlet} - C_{exit,NO})/C_{inlet}$, where C_{inlet} is the inlet concentration of NO. Oxidation was carried out in presence of O_2 (20%, v/v) and at a reaction temperature of 30 °C. The inlet NO and gas flow rate were kept constant at 300 ppm and 0.2 slpm. As observed from the figure, breakthrough occurred instantly. Following breakthrough, the exit NO concentration increased upto the level of 55% (corresponding to the conversion ~45%) before increasing to the steady-state conversion of ~55%. Refer the transient data for NO_2 shown in Fig. 4. The time period during which NO concentration increased, NO_2 formed due to oxidation was adsorbed completely. NO_2 breakthrough was observed after ~250 min from the start of test run. NO concentration reached maximum level at ~250 min, when breakthrough of NO_2 occurred.

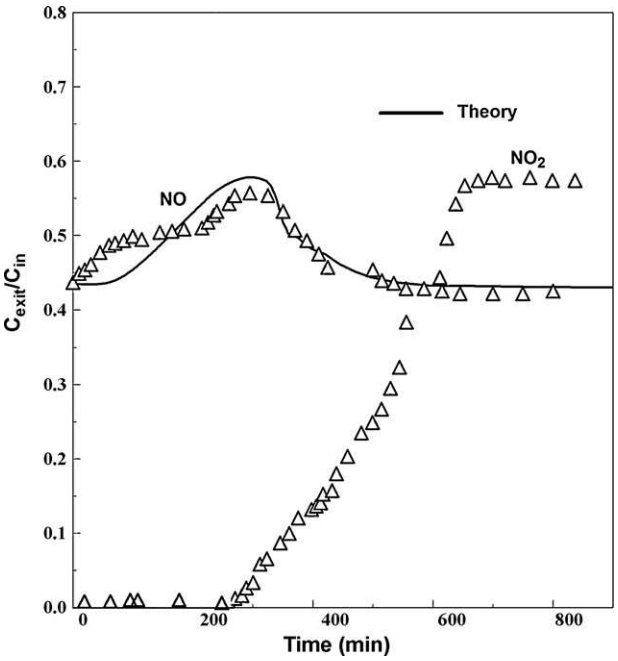

Fig. 4. Oxidation of No over non-functionalized ACF (W = 0.5 g, Q = 200 sccm, NO = 300 ppm, O_2 = 20% (v/v) and T = 30 °C).

Fig. 4 also describes the theoretical curve (shown by solid line) calculated under the identical conditions as used for the experimental data. In our previous study, a kinetic mechanism was proposed on the oxidation of NO by non-functionalized ACF [20]. The aforementioned study also included a transport model to predict the transient concentration data of NO during the flow through the packed bed of non-functionalized ACF. We have used the same model to explain the present data on the oxidation of NO by functionalized ACF. While the details of the proposed kinetics and the model may be obtained from the aforesaid study, we briefly discuss those for elucidation of the data. It is important to recall from our previous discussions that the oxidation of NO on the non-functionalized ACF differs from that on the (NH_3-) functionalized ACF in that surface functional groups facilitate the adsorption of NO. Therefore, in principle, the general kinetic steps for the adsorption/desorption and oxidation of NO on two surfaces (with and without functionalized) are similar, as shown below. The difference, however, arises in the numerical values of the kinetic parameters corresponding to the functionalized and non-functionalized surfaces of ACF.

The mathematical model for the unsteady-state concentration of NO in the ACF-packed tubular reactor essentially includes three mechanistic steps: (1) mass transfer of NO from the gas phase in the packed bed to the outer surface of fibers, (2) diffusion of NO within the pores, and (c) oxidation on the surface inside the pores. Three species balance equations are accordingly derived for the three aforementioned steps and solved with the appropriate initial and boundary conditions corresponding to the existing experimental conditions. The detailed mathematical steps may be obtained from the reference [20].

Under the present case studied, the effective pore diffusivity (D_{eff}) was calculated to be 1.8×10^{-8} m^2/s. The numerical value of D_{eff} is in the same order of magnitude as reported elsewhere for the pore-diffusion of organic species and SO_2 in ACF [12,13]. At the gas flow rate of 200 sccm, Re (based on the fiber diameter of 2.8×10^{-6} m) and Sc were calculated to be 0.0085 and 0.014, respec-

tively. Under these conditions, *Sh* was calculated to be 2.015, which in turn was used to calculate the gas film mass transfer coefficient, k_m (652.8 m/s) based on the available correlations [21]. The relatively larger value of k_m suggests the insignificant film mass transfer diffusional resistance in the bed packed with ACF.

In the mechanism for the oxidation of NO by ACF, we have assumed the Langmuir–Hinshelwood model. The gaseous NO and O_2 are assumed to adsorb on the active sites of ACF, followed by oxidation of NO into adsorbed NO_2. The adsorbed NO_2 may further react and form various intermediates such as, NO_3 and NO-NO_3 in adsorbed phase. Finally, the adsorbed intermediate NO-NO_3 is desorbed into NO_2 from the surface, thereby releasing the vacant sites for the adsorption of successive molecules of adsorbates: The overall sequential reactions may be written as follows:

$$NO + C_f \underset{k_{-1}}{\overset{k_1}{\rightleftharpoons}} C\text{-}NO \quad (a)$$

$$O_2 + 2C_f \underset{k_{-2}}{\overset{k_2}{\rightleftharpoons}} 2C\text{-}O \quad (b)$$

$$C\text{-}NO + C\text{-}O \underset{k_{-3}}{\overset{k_3}{\rightleftharpoons}} C\text{-}NO_2 + C_f \quad (c)$$

$$C\text{-}NO_2 + C\text{-}NO_2 \underset{k_{-4}}{\overset{k_4}{\rightleftharpoons}} C\text{-}NO_3 + NO + C_f \quad (d)$$

$$C\text{-}NO_3 + C\text{-}NO \underset{k_{-5}}{\overset{k_5}{\rightleftharpoons}} C\text{-}NO\text{-}NO_3 + C_f \quad (e)$$

$$C\text{-}NO\text{-}NO_3 \xrightarrow{k_6} 2NO_2 + C_f \quad (f)$$

Here, k_i and k_{-i} (i = 1–5) are the forward and backward reaction rate constants of respective reactions. C_f denotes the vacant sites, whereas C-NO, C-O, C-NO_2, C-NO_3 and C-NO-NO_3 represent the adsorbed species on the surface of ACF. Assuming that desorption of NO_2 (reaction (f)) is the rate limiting step, the apparent rate of overall reaction may be written as follows:

$$\frac{1}{2}\frac{dC_{NO_2}}{dt} = \frac{-1}{2}\frac{dC_{NO}}{dt} = k_6[C\text{-}NO\text{-}NO_3] \quad (1)$$

The assumption of the kinetic step (f) as the rate limiting step is consistent with the observed experimental data as explained in the subsequent paragraph. As a consequence of this assumption, reactions (a)–(e) may be assumed to be in quasi-equilibrium, and the (pseudo) steady-state concentrations of different adsorbed species may be obtained by equating the forward and backward rates of the respective equations. In addition, the conservation equation for total number of sites [C_t] may be written as follows:

$$[C_t] = [C_f] + [C\text{-}O] + [C\text{-}NO] + [C\text{-}NO_2] + [C\text{-}NO_3] + [C\text{-}NO\text{-}NO_3] \quad (2)$$

Substituting the concentrations of the intermediate species in terms of the reacting species, it is trivial to recast Eq. (1) for the rate of the removal of NO as:

$$\frac{-1}{2}\frac{dC_{NO}}{dt} = \frac{K_{11}{C_{NO}}^2}{K_{22} + K_{33}C_{NO} + K_{44}{C_{NO}}^2} \quad (3)$$

where, K_{11}, K_{22}, K_{33}, and K_{44} are the terms containing the equilibirum constants of the reaction steps (a)–(e) and the concentration of oxygen. Since NO concentration in the inlet stream is smaller compared to O_2, we may neglect higher order ${C_{NO}}^2$ term and assume C_{O_2} to be constant. Therefore, Eq. (3) is further simplified as follows:

$$\frac{-1}{2}\frac{dC_{NO}}{dt} = \frac{rc_1{C_{NO}}^2}{1 + rc_2C_{NO}} \quad (4)$$

where,

$$rc_1 = K_{11}/K_{22} \text{ and } rc_2 = K_{33}/K_{22} \quad (5)$$

From the above equations, it is trivial to infer that the rate of change of NO concentration has complex dependencies on the concentration levels of the reacting species (NO and O_2).

Re-refer Fig. 4. We may explain the breakthrough characteristics of NO and NO_2 with the aid of the proposed mechanism discussed above. The sharp rise in the outlet concentration of NO during the initial period indicates that the physical adsorption and desorption of NO, i.e. step (a) of the proposed mechanism is slower compared to the remaining steps, which are quite rapid, i.e. at quasi-equilibrium conditions. Therefore, during the initial period the adsorption of NO is the rate-determining step. When the bed begins to saturate with NO and/or NO_2, we may observe large increase in the outlet concentration of NO, which reaches to a maximum value. At the same time breakthrough of NO_2 occurs, which results in release of the vacant sites, C_f, consistent with the reaction step (f) of mechanism 1. Hence, adsorption of NO may again take place on these vacant sites, so that there will be a gradual decrease in the outlet concentration of NO before reaching the steady-state level, as observed from the data. In other words, adsorption of NO on the new vacant sites proceeds only when NO_2 is desorbed to release these sites, which then becomes the slower step. Therefore, during this time period, desorption of NO_2 is the rate limiting step, i.e. the step (f) of the proposed mechanism. The extent of physical adsorption of NO on activated carbons is generally small because NO is a supercritical fluid at the ambient temperature, limited due to its weak interactions with the adsorbate (ACF in the present case) [22]. Thus, the adsorbed NO is first oxidized to NO_2, which in turn may be removed by the other commercially available adsorbents, such as silica gel and activated carbon.

Fig. 4 also presents the model predicted breakthrough curve of NO along with the corresponding experimental data under the identical operating conditions. From the discussion of the kinetics in the preceding texts, it is clear that the reaction rate coefficients, rc_1 and rc_2 are the two adjustable parameters in the model and have complex dependency on the concentrations of the reactants, intermediate and product species. These model parameters were accordingly adjusted to explain the data. As mentioned earlier, the other two transport parameters, effective pore diffusivities and mass transfer coefficients were calculated from the literature correlations. As observed from the data, the breakthrough of NO took place much earlier than the detection of NO_2 at the exit of the reactor, suggesting that the NO adsorption was rate-determining step until increase in the NO_2 concentration in the gas phase begun sharply. Therefore, if the breakthrough time of NO_2 is t_1, we may infer that till time t_1, the overall oxidation of NO is controlled by the physical adsorption of NO, whereas after t_1, desorption of NO_2 is rate controlling. Thus, during time t_1, an assumption of quasi-equilibrium is made, where change in the surface phase NO concentration due to that in the gas phase concentration is assumed to be rapid or instant. After time t_1, the oxidation rate is determined as per the rate expression Eq. (4). As observed from the figure, there is a reasonably good agreement between the data and the model predictions.

2.3.2. NH_3 functionalized ACF: effect of aq. NH_3 concentration

Fig. 5(a and b) illustrate the effect of NH_3 concentration on the oxidation of NO by ACF. ACF was functionalized with three different aqueous ammonia concentrations as per the procedure described in the Section 2.1.2. As observed, breakthrough of NO occurred approximately around the same time (~4 min) for all three samples. The maximum exit NO concentration was in the following order: ACF-NH_3/10 M (60%) > ACF-NH_3/3 M (50%) > ACF-NH_3/5 M (45%). As also observed, the maximum steady-state NO conversion (~70%)

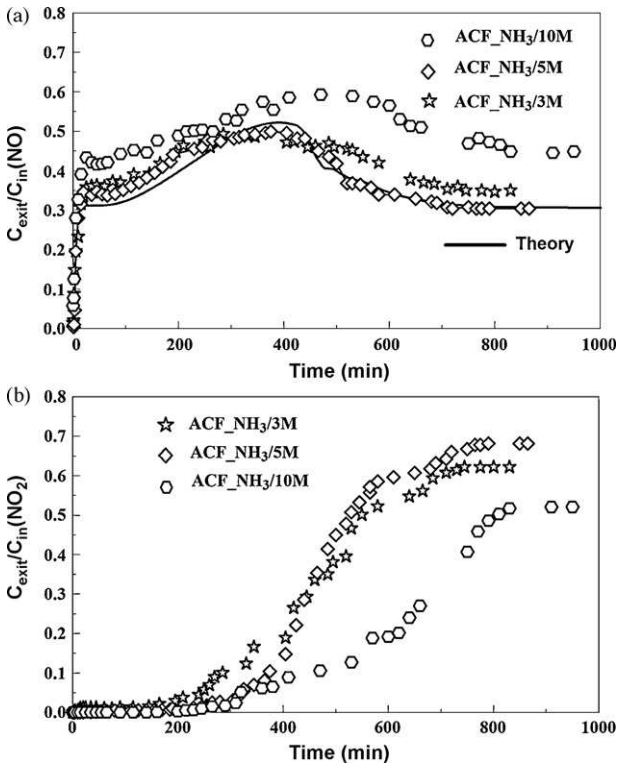

Fig. 5. Effect of different ammonia concentrations on (a) the oxidation of NO (top), (b) breakthrough of NO_2 (bottom) (W = 0.5 g, Q = 200 sccm, NO = 300 ppm, C_{O_2} = 20% and T = 30 °C).

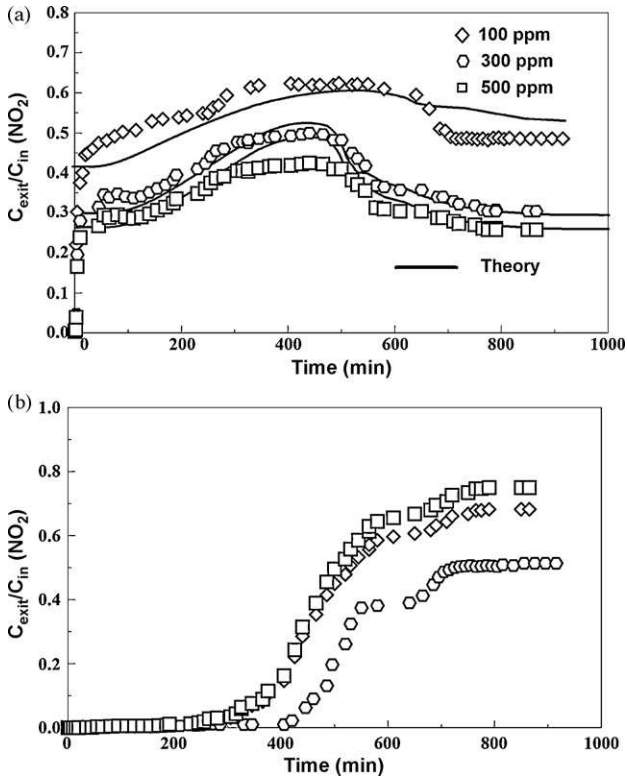

Fig. 6. Effect of inlet NO concentrations on the (a) oxidation of NO (top), (b) breakthrough of NO_2 (W = 0.5 g, Q = 200 sccm, C_{NH_3} = 5 M, C_{O_2} = 20% and T = 30 °C).

occurs for the ACF sample impregnated with the 5 M aqueous NH_3 solution. The relatively larger NO conversion for ACF-NH_3/5 M sample is attributed to the presence of large number of N-containing groups. Similar to the observations made in Fig. 4 for the non-functionalized ACF, breakthrough of NO_2 occurred around the same time the maximum NO exit concentration occurs. As observed from the figure, the agreement between the data corresponding to the ACF-NH_3/5 M sample and the theory calculations is reasonable. To explain the model calculated curve shown in Fig. 5 for the surface functionalized ACF with 5 M NH_3, the basic postulate of the model was considered to be the same for the curve obtained for the non-functionalized ACF. The two parameters, rc_1 and rc_2, were, however, adjusted to fit the data.

2.3.3. Aq. NH_3 functionalized ACF: effect of NO concentration

To ascertain the effect of NO inlet concentrations on the oxidation of NO, the experiments were carried out for three NO concentrations: 100, 300 and 500 ppm. Oxidation was carried out in the presence of O_2 (20%, v/v) and at the room temperature of 30 °C. Fig. 6(a and b) illustrate the breakthrough profiles of NO. As observed, time to reach maximum concentration of NO decreased with increasing NO concentration. In addition, the maximum NO concentration level also decreased. On the other hand, the breakthrough time of NO_2 decreased from ~400 to 300 min with increasing concentration. The corresponding steady-state conversions were observed to be ~50 and 70% respectively. There was marginal difference observed between the breakthrough data corresponding to 300 and 500 ppm of NO concentrations.

Fig. 6 also shows the model predicted breakthrough curves for three NO concentrations (100, 300, and 500 ppm), which are observed to be reasonably in good agreement with the experimental data. In the model predictions, the numerical values of rc_1 and rc_2 were expectedly set unchanged (the same as those chosen for the model curve for the data shown on Fig. 5), i.e. independent of NO concentration. Re-visit the section on kinetics of NO oxidation, in particular Eq. (4). The two model parameters, rc_1 and rc_2, are dependent on the equilibrium rate constants and oxygen concentration. The latter was set constant at 20% for all test runs. Thus, variation in the model parameters is consistent with the data. While the NO oxidation rate has non-linear dependency on NO concentration, the rate parameters are dependent on temperature and oxygen concentration.

2.3.4. Surface functionalized ACF: effect of different reagents

Fig. 7(a and b) compares the performance of ACF functionalized with aq. NH_3 solution (5 M) to that functionalized with vapor NH_3. Amongst the other functionalization agents used in the study, pyridine was found to be the most effective and is accordingly included in the figure for comparison. However, we did not find any significant oxidative effects on ACF functionalized with diethylamines, in which case the breakthrough of NO occurred instantaneously, reaching the inlet concentration, without any appreciably measured conversion. As shown in the figure, NO conversion is largest in the case of ACF-NH3-l sample compared to other two samples, with the steady-state conversion observed as follows: ACF-NH3-l (~70%) > ACF-NH3-v (~60%) > ACF-pyridine (~58%). The salient observation to note is the superior performance of ACF impregnated via liquid phase than the vapor phase. Using all other reagents for impregnation, including amines and pyridine, we repeatedly observed identical trend in the oxidative removal of NO, suggesting that nitrogen doping (incorporation of nitrogen groups) on ACF is more effective at room temperature than at large temperature. We attribute reduced performance of ACF prepared by vapor phase impregnation due to excessive condensation resulting in pore-blocking, in line with the observation made elsewhere [23].

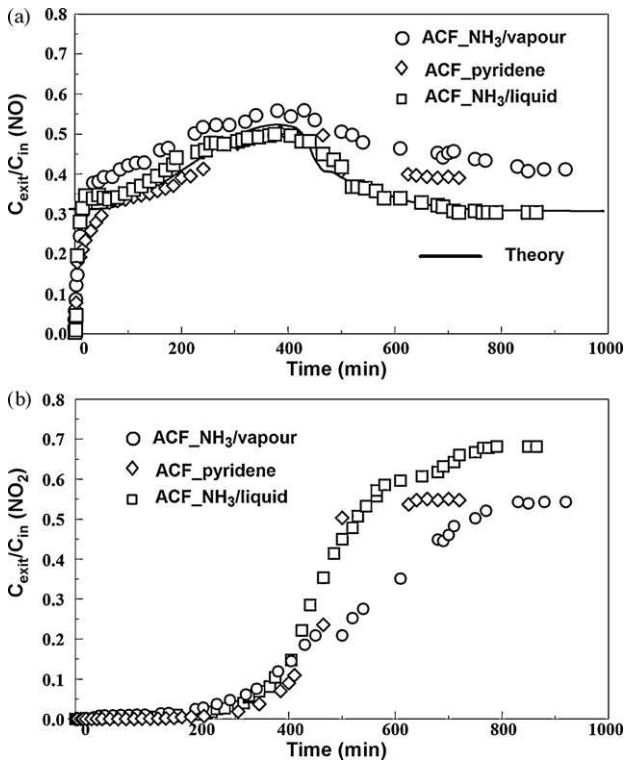

Fig. 7. Effect of different reagents on the (a) oxidation of NO (top), (b) breakthrough of NO_2 (bottom) ($C_{NH_3} = 5$ M, $Q = 200$ sccm, NO = 300 ppm, $C_{O_2} = 20\%$ and $T = 30\,^{\circ}C$).

3. PM capture in engine exhaust

3.1. Experimental set-up

In this investigation a typical transport engine (Make: Mahindra & Mahindra, India, Model: XD-3P) was used. This is a four-cylinder, water-cooled, indirect-injection, diesel engine, coupled with an eddy current dynamometer. The dynamometer (Make: Schenck Avery, India, Model: ASE-50,) is equipped with a dyno controller capable of loading the engine at the desired speed and load combination. Detailed specifications of the engine are given in Table 2.

Fig. 8 is the schematic of the experimental set-up used to study control of PM using the functionalized ACF (prepared in this study)

Table 2
Specifications of diesel engine used in the experiment.

Model	Mahindra XD-3P
Type	Water-cooled, four-stroke
Number of cylinders	4
Compression ratio	23:1
Bore diameter	94 mm
Stroke length 90 mm	90 mm
Power output	72.5 hp @4000 rpm without oil cooler
Max. torque	125 N-m @ 2000 rpm
Loading device	Eddy current dynamometer (Model: ASE-50 Make: Shank Avery)

for trapping particulates. The entire set-up may be assumed to consist of three sections: (a) partial exhaust inlet, (b) test section, and (c) analytical sections. To characterize PM, a part of the engine exhaust was withdrawn from the main exhaust line. This partial exhaust was allowed to pass through a magnetic rotameter to measure the flow rate. Desired flow rate of exhaust was maintained using a manual control valve provided at the bottom of the rotameter. The test section consisted of a horizontal tubular reactor made of stainless steel (SS). The reactor essentially consisted of two parts: a perforated SS tube (1/2 in. × 5 in.) mounted in a SS shell (1.5 in. × 8 in.). The heating to the reactor was provided by a tubular electric furnace (1000 W) with a thermocouple placed directly in contact with the reactor inside the furnace. The temperature of the reactor was controlled using a PI controller. The analytical section consisted of an Engine Exhaust Particle Sizer (EEPS) (Make: TSI, USA; Model: 3090) to characterize the particulate number-size, area and volume distribution. There was an option of bypassing this engine exhaust directly to the EEPS.

EEPS spectrometer provides both high temporal resolution and reasonable size resolution with multiple detectors working in parallel. This makes the EEPS ideal for measuring engine operating under transient conditions. EEPS is designed specifically to measure particulate emitted from engines and vehicles. It measures particle size from 5.6 to 560 nm with a size resolution of 16 channels per decade (a total of 32 channels). Reading the particle size distribution 10 times per second (10 Hz) allows even transient measurement possible.

Diesel particulate enters the instrument through a cyclone with a 1 μm cut-off limit. This removes large particles that are above the instrument's measurement capabilities. These particulate then pass through an electrical diffusion charger, in which ions are generated.

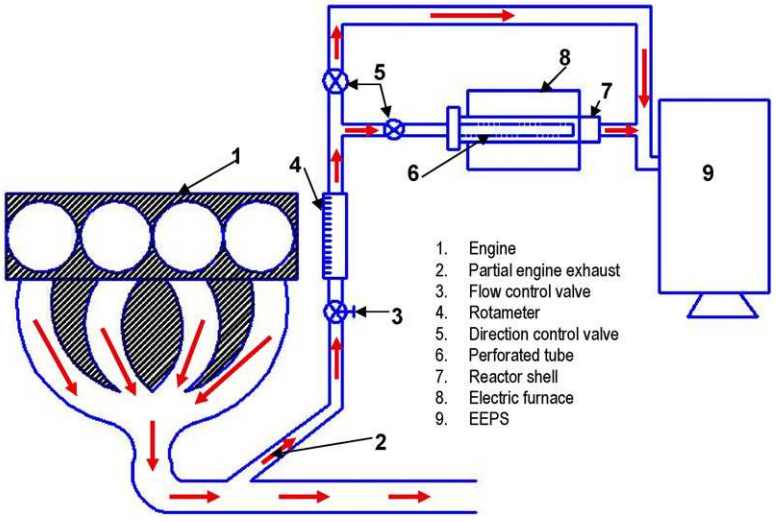

Fig. 8. Schematic of the experimental set-up used for the PM control study on diesel exhaust.

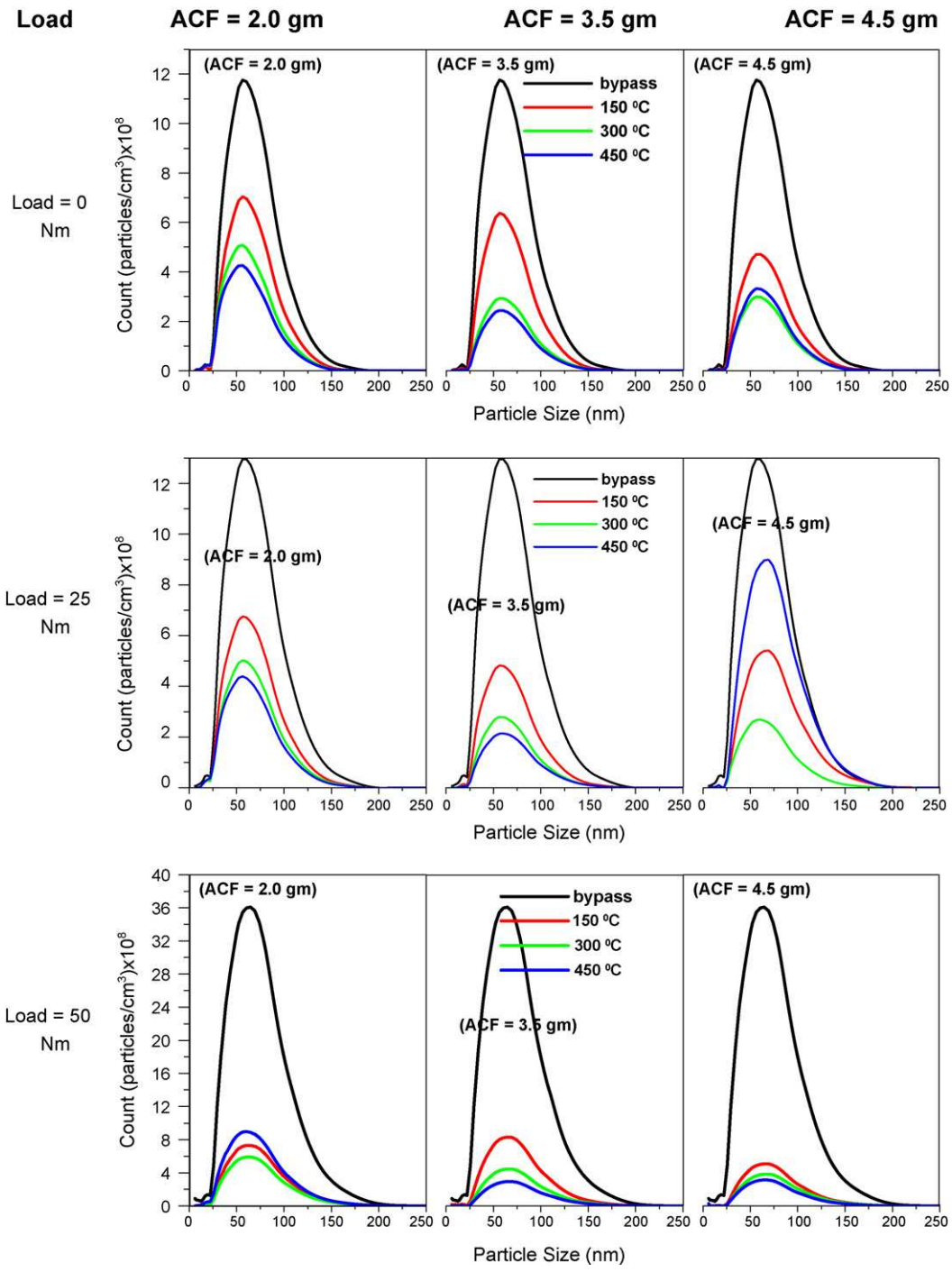

Fig. 9. Particulate density distribution vs. size at different engine loads and amounts of ACF.

These ions mix with the particulate to provide a predictable charge based on their surface area. The charged particulate then enters an annular space between two cylinders which is filled with clean sheath air. The particles pass by a central rod that has a high voltage to produce an electric field which repels the particulate outward to the electrometer rings. The particles are collected on electrometer rings transferring their charge to a sensitive electrometer on each ring depending on their size. Small particles are detected at the top of the column and larger particles at the bottom due to its inertia. The electrometers are read at 10 Hz frequency by a microprocessor, which then inverts the current data to get particle size and number distribution.

3.2. Experimental procedure

All tests were carried out at constant engine speed of 2000 rpm. Particulate concentration, and surface area distribution were measured at three different engine load (0, 25 and 50 Nm). Reactor temperature was varied from 150 to 450 °C to identify the effect of temperature on particulate concentration. Particulate size was measured for bypass exhaust and the exhaust coming out from reactor (ACF) to compare the performance of ACF. Since the total number of particulate present in raw exhaust is significantly higher than the number that instrument can handle, it was diluted with clean sheath air. Dilution of the exhaust gas was done using rotating

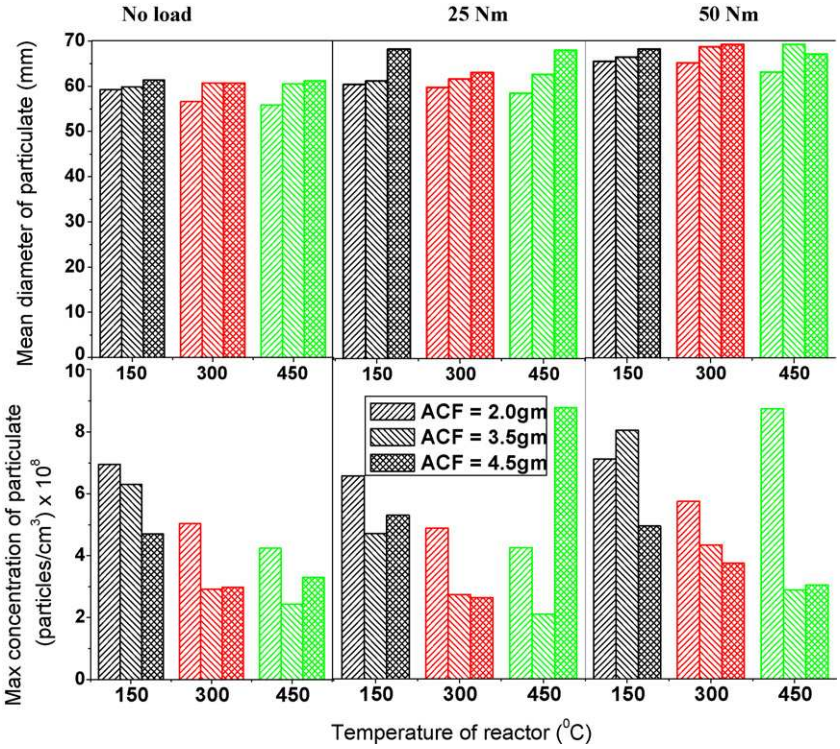

Fig. 10. Mean diameter and maximum density of particulate at different engine loads and amounts of ACF.

disc diluter (Make: Matter Engineering AG, UK; Model: 379030) to lowers particle concentration to a value within the measurement range of the EEPS. For the present set of experiment, exhaust gas was diluted by a dilution ratio of 518:1.

The removal of PM using ACF is based on the principal of capturing and subsequent oxidation of collected PM. In this process, PM gets converted into CO_2, which is relatively harmless compared to PM. The prepared ACF (3.5 g) sample was wrapped over a perforated tube in a tubular reactor surrounded by a shell. Experiments were carried out at varying engine loads 0–80% and at constant engine speed of 1800 rpm. The reactor was heated to desired reaction temperature (450 °C) and further kept at that temperature for another 30 min so that the system was stabilized and a uniform temperature is maintained in the packed bed reactor. The constant flow of exhaust (1.3 m^3/h) was maintained. Initially the exhaust flow was bypassed to measure the inlet smoke opacity by smoke meter. Then the flow was allowed to pass through the reactor surrounded with an electric furnace and the exit particle concentrations were measured by EEPS.

3.3. PM data (number and surface area density distribution)

Fig. 9 describes the distribution of particulate concentration (number density) vs. size at different engine operating conditions (varying engine loads and amounts of ACF). In each case, PM concentration distributions of engine exhaust were measured downstream of the reactor at three different temperatures, 150, 350 and 450 °C and compared to those obtained in the tube bypassing the reactor. Here, we discuss the representative results on the characteristic variation observed in the number and surface area density distributions due to variation in the operating conditions.

As observed from the figure, particulate concentrations at the exit of the reactor are consistently smaller than those in the tube bypassing the reactor. At no load condition, reactor temperature of 150 °C and ACF amount of 2 g, the peak (maximum) concentration of PM in the bypass line is measured to be 1.17×10^9 particles/cm^3 in comparison to 6.95×10^8 particles/cm^3 at the exit of the reactor. Thus, there is approximately 40% reduction in the peak concentration of PM compared to the bypass line. As also observed, the mode of the particulate size is shifted from 60.4 to 52.3 nm. As the reactor temperature was increased from 150 to 450 °C, peak concentration decreased from 6.95×10^8 to 4.24×10^8 particles/cm^3. At 450 °C, the overall reduction in peak concentration downstream of the reactor was observed to be approximately 64% relative to that measured in the bypass line. As load on the engine is increased from no load to 25 Nm, there is further reduction observed in the peak concentration of PM in the exhaust line corresponding to all three reactor temperatures. However, there is a shift in the mode size of PM from 52.3 to 60.4 nm. The trend in the data corresponding to the larger amounts of ACF used in the reactor is similar and not discussed for brevity.

From the foregoing data, we observe that the size distribution of particulate increases with increasing engine load. The distribution broadening has major effect on the right side of the size distribution. With the relatively higher engine load, the temperature and the amount of injected fuel are largest, whereas the air to fuel ratio is smallest. These conditions result in the increase of the initial soot formation and also accelerate the agglomeration of PM. Furthermore, the size distribution of the PM is smaller at the exit of the reactor than in the exhaust bypass.

Experiments were also carried out to ascertain the effect of amount of ACF, as shown in Fig. 9. For comparative analysis, the salient results, essentially the data on the mean diameter and the maximum concentration of PM observed at various engine operating loads and amounts of ACF are presented in Fig. 10. As observed, at no load condition, peak concentration of PM decreased as the amount of ACF in the reactor was increased. However, at the reactor temperature of 450 °C, adverse effect was occasionally observed, which was attributed to the burn-out of ACF at relatively higher temperatures. The notable observation is the variation in the mean diameter of PM over a narrow band between 56 and 67 nm.

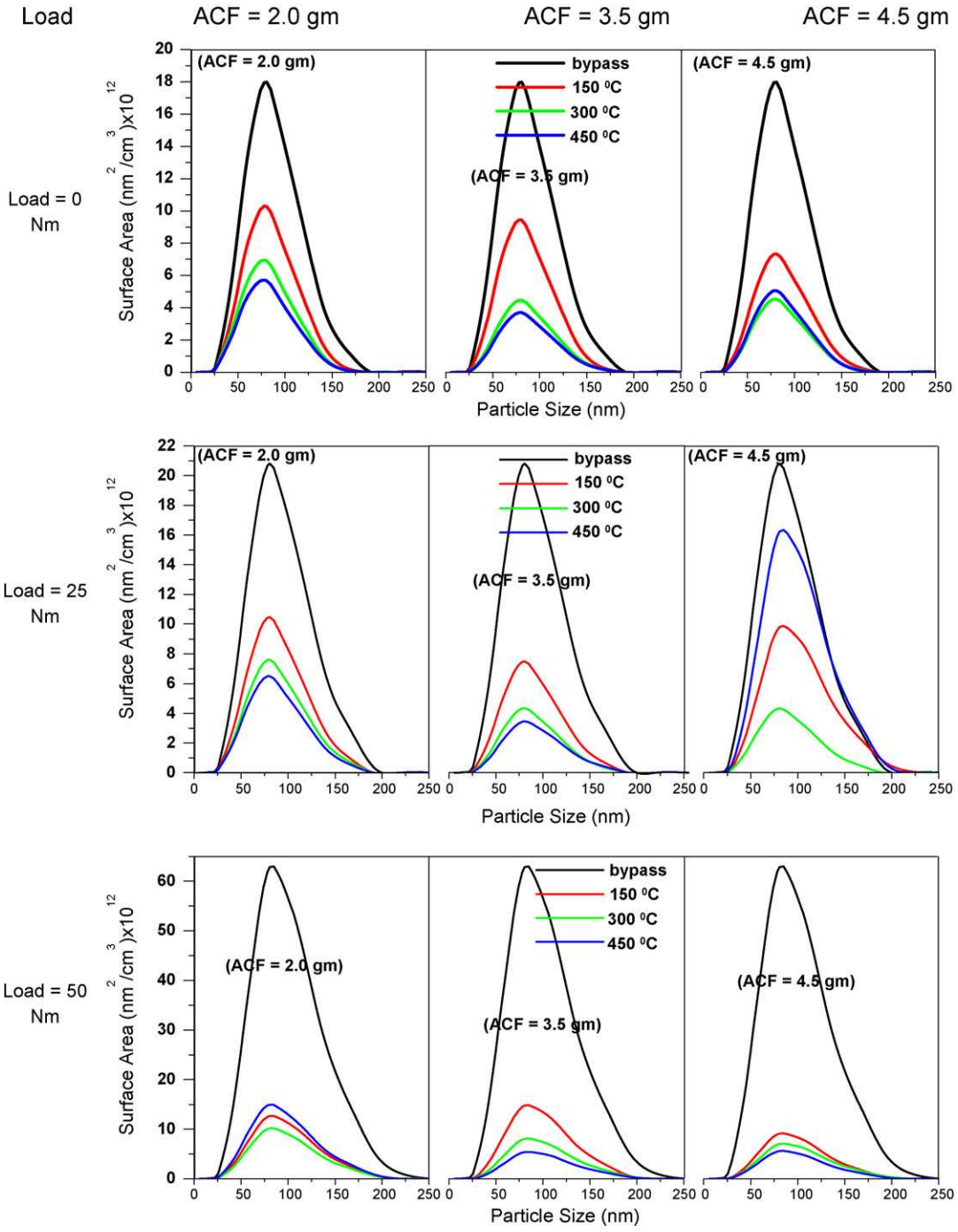

Fig. 11. Surface area of Particulate distribution vs. size at different engine load and ACF weight.

The data on the surface area distribution is important from the perspective of toxicology of the PM emitted from the engine. In general, surface area of the particulate determines the extent at which it interacts with the environment. This may involve the (photo)-chemical reaction, gas-to-particle conversion, liquid adsorption/desorption and particle-solid interaction. By such mechanisms, particles transform and age in the atmosphere and act on the human body. It should be expected that relevant effects become more prominent as surface area increases. This becomes even more important when a specific surface area is considered, e.g. per particle mass or number concentration.

Fig. 11 describes the surface area distribution vs. size of particulate at different engine loads and the amounts of ACF, analogous to the data presented in Fig. 9 for particle number density. As observed, the peak surface area distribution decreases with increasing reaction temperature. At no load engine condition, the smallest surface area distribution was obtained at 3.5 g of ACF and the reaction temperature of 450 °C, although occasional burn-out of ACF occurred at or near 450 °C. The peak surface area of particulate in the bypass line is 18×10^{13} nm^2/cm^3 in comparison to 3.7×10^{12} nm^2/cm^3 obtained at the exit of the reactor packed with 3.5 g of ACF. Thus, there is 80% reduction in the peak surface area distribution of PM. Interestingly it was observed that the mode size of surface area was constant at 80.6 nm in all experimental conditions. Fig. 12 sums up the mean diameter of the surface area distribution and maximum surface area, the two parameters eval-

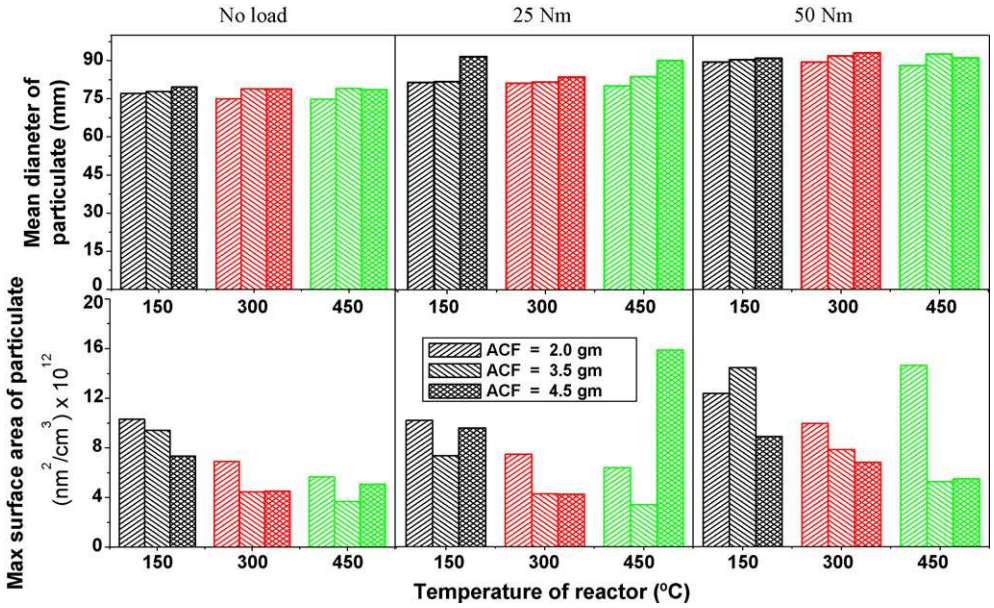

Fig. 12. Mean diameter and maximum surface area density of particulate at different engine load and ACF weight.

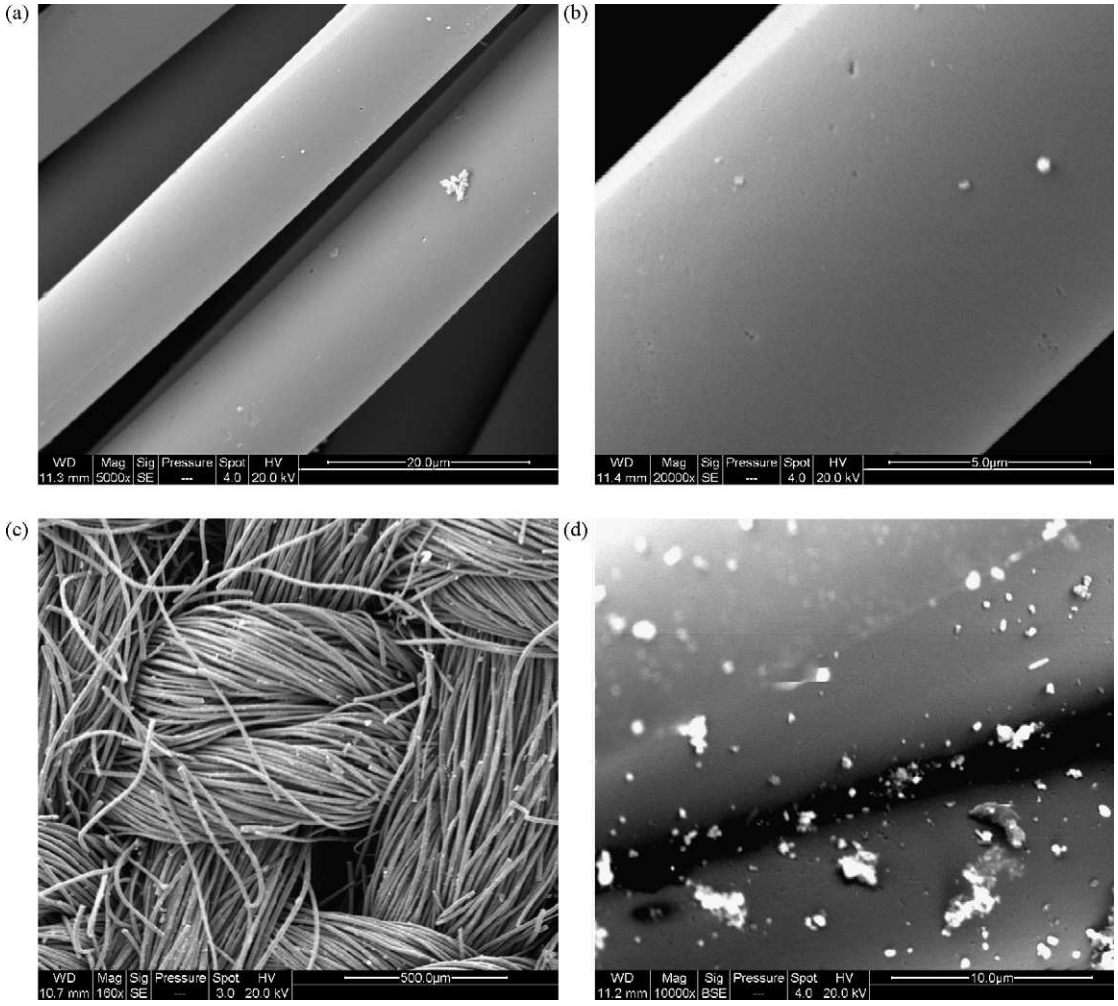

Fig. 13. SEM images of ACF: (a) and (b) untreated samples at 5000× and 20,000× magnifications, respectively, and (c) and (d) post-test surface functionalized samples 150× and 10,000× magnfications, respectively.

uated from the data shown on Fig. 11. The mean particle size is observed to vary from 74.8 to 90.6 nm, as the engine operating condition is changed from no-load to 50 nm.

Finally, visible inspection and the SEM analysis of the ACF samples were carried out to physically ascertain any perceptible deterioration of the surface of ACF following NO oxidation and engine tests in this study. No visible deterioration was observed in the physical appearance and strength of ACF. Fig. 13 describes the representative SEM images of the ACF samples following those tests. As observed, integrity of the fibers is intact. In this context, it is also appropriate to point out that we have carried out a number of SEM analysis on the phenolic resin precursor based ACF samples in our previous studies related to adsorption/catalytic oxidation applications. In these studies, the ACF samples were subjected to significantly larger temperature (∼1000 °C) during processing than that in the present study. However, similar to the present case, no deterioration of the surface of the fiber was observed [24].

4. Conclusions

The ACF functionalized with NH_3 was tested for NO oxidation and particulate removal in the exhaust gas from a diesel engine. Approximately 70% conversion was achieved during the oxidation of NO. The relatively larger NO adsorption was observed on ACF-NH_3/5 M due to the presence of more N-containing groups. In addition, nitrogen doping on ACF at room temperature was found to be more effective than at the high temperature. The prepared samples were observed to be promising in capturing particulate matters from the engine exhaust as well. Approximately ∼90% reduction in the particle concentration was achieved using NH_3 impregnated ACF, with number density and surface area distribution of particulate at the exit of the reactor consistently found to be lower than those in the bypass engine exhaust. Mean diameter of particulate concentration was observed in the narrow band of 56–67 nm. The experimental data suggest the prepared ACF samples in this study as a potential material to control the emission of NO and PM.

References

[1] IPCC, Climate Change- Mitigation, Third Assessment Report, Intergovernmental Panel on Climate Change, Cambridge University Press, UK, 2001.
[2] J.L. Mauderly, Diesel emissions: is more health research still needed? Toxicol. Sci. 62 (1) (2001) 6–9.
[3] S. Abdul, D. Kittelson, B. Graskow, Q. Wei, Diesel exhaust particle size measurement issues and trends, SAE paper 980525 (1998).
[4] D. Dwivedi, A.K. Agarwal, M. Sharma, Particulate emission characterization of a biodiesel vs diesel fuelled compression ignition transport engine: a comparative study, Atmos. Environ. 40 (2006) 5586–5595.
[5] M. Sharma, A.K. Agarwal, K.V.L. Bharathi, Characterization of exhaust particulates from diesel engine, Atmos. Environ. 39 (2005) 3023–3028.
[6] E. Cauda, D. Fino, G. Saracco, V. Specchia, Preparation and regeneration of a catalytic diesel particulate filter, Chem. Eng. Sci. 62 (2007) 5182.
[7] P. Hawker, J. Henn, W. Koch, G. Huthwohl, Effect of continuously regenerating diesel particulate filter on non-regulated emissions and particle size distribution, SAE paper 980189 (1998).
[8] T. Kojima, A. Tange, K. Tamatsu, Developments of diesel particulate filter systems with mesh laminated structures, JSAE Rev. 20 (1999) 117.
[9] D. Das, V. Gaur, N. Verma, Removal of volatile organic compound by activated carbon fiber, Carbon 42 (2004) 2949.
[10] V. Gaur, A. Sharma, N. Verma, Catalytic oxidation of toluene and m-xylene by activated carbon fiber impregnated with transition metals, Carbon 43 (2005) 3041.
[11] V. Gaur, N. Verma, Preparation and characterization of ACF for the adsorption of BTX and SO_2, Chem. Eng. Process. 45 (2006) 1.
[12] T. Cheng, Y. Jiang, Y. Zhang, S. Liu, Prediction of breakthrough curves for adsorption on activated carbon fibers in a fixed bed, Carbon 42 (15) (2004) 3081–3085.
[13] V. Gaur, R. Asthana, N. Verma, Removal of SO_2 by activated carbon fibers in presence of O_2 and H_2O, Carbon 44 (2006) 46–60.
[14] L. Mangun, R. Benak, J. Economy, J. Foster, Surface chemistry, pore sizes and adsorption properties of activated carbon fibers and precursors treated with ammonia, Carbon 39 (2001) 1809.
[15] E. Raymundo-Piñero, D. Cazorla-Amorós, A. Linares-Solano, The role of different nitrogen functional groups on the removal of SO from flue gases by N-doped activated carbon powders and fibres, Carbon 41 (2003) 1925–1932.
[16] L. Xu, J. Guo, F. Jin, H. Zeng, Removal of SO_2 from O_2-containing flue gas by activated carbon fiber (ACF) impregnated with NH_3, Chemosphere 04 (2006) 70.
[17] H. Tamai, K. Shiraki, T. Shiona, H. Yasuda, Surface functionalization of mesoporous and microporous activated carbons by immobilization of diamine, J. Colloid Interface Sci. 295 (2006) 299.
[18] C. Yang, K. Kaneko, Nitrogen-doped activated carbon fiber as an applicant for NO adsorbent, J. Colloid Interface Sci. 255 (2002) 236.
[19] William Kemp, Organic Spectroscopy, 2nd ed., Palgrave, New York, 1991.
[20] S. Adapa, V. Gaur, N. Verma, Catalytic oxidation of NO by activated carbon fiber, Chem. Eng. J. 116 (2006) 25.
[21] R.T. Yang, Gas Separation by Adsorption Processes, 1st ed., Imperial College, UK, 1997.
[22] Z.M. Wang, T. Suzuki, N. Uekawa, K. Asakura, K. Kaneko, Mixed valence oxide-dispersion-induced micropore filling of supercritical nitric oxide, J. Phys. Chem. 96 (26) (1992) 10917–10922.
[23] Y. Chiang, C. Lee, H. Lee, Surface chemistry of polyacrylo-nitrile and rayon based activated carbon fibers after post-heat treatment, Mater. Chem. Phys. 101 (2007) 199–206.
[24] V. Gaur, A. Sharma, N. Verma, Removal of SO_2 by activated carbon fiber impregnated with transition metals, CJChE 85 (2007) 1–11.